High-Resolution Spatial Modeling of Daily Weather Elements for a Catchment in the Oregon Cascade Mountains, United States

CHRISTOPHER DALY, JONATHAN W. SMITH, AND JOSEPH I. SMITH

Oregon State University, Corvallis, Oregon

ROBERT B. MCKANE

U.S. Environmental Protection Agency, Corvallis, Oregon

(Manuscript received 7 August 2006, in final form 8 January 2007)

ABSTRACT

High-quality, daily meteorological data at high spatial resolution are essential for a variety of hydrologic and ecological modeling applications that support environmental risk assessments and decision making. This paper describes the development, application, and assessment of methods to construct daily high-resolution (~50-m cell size) meteorological grids for the 2003 calendar year in the Upper South Santiam Watershed (USSW), a 500-km^2 mountainous catchment draining the western slope of the Oregon Cascade Mountains. Elevations within the USSW ranged from 194 to 1650 m. Meteorological elements modeled were minimum and maximum temperature; total precipitation, rainfall, and snowfall; and solar radiation and radiation-adjusted maximum temperature. The Parameter–Elevation Regressions on Independent Slopes Model (PRISM) was used to interpolate minimum and maximum temperature and precipitation. The separation of precipitation into rainfall and snowfall components used a temperature-based regression function. Solar radiation was simulated with the Image-Processing Workbench. Radiation-based adjustments to maximum temperature employed equations developed from data in the nearby H. J. Andrews Experimental Forest. The restrictive terrain of the USSW promoted cold-air drainage and temperature inversions by reducing large-scale airflow. Inversions were prominent nearly all year for minimum temperature and were noticeable even for maximum temperature during the autumn and winter. Precipitation generally increased with elevation over the USSW. In 2003, precipitation was nearly always in the form of rain at the lowest elevations but was about 50% snow at the highest elevations. Solar radiation followed a complex pattern related to terrain slope, aspect, and position relative to other terrain features. Clear, sunny days with a large proportion of direct radiation exhibited the greatest contrast in radiation totals, whereas cloudy days with primarily diffuse radiation showed little contrast. Radiation-adjusted maximum temperatures showed similar patterns. The lack of a high-quality observed dataset was a major issue in the interpolation of precipitation and solar radiation. However, observed data available for the USSW were superior to those available for most mountainous regions in the western United States. In this sense, the methods and results presented here can inform others performing similar studies in other mountainous regions.

1. Introduction

There is a growing need for high-quality, daily meteorological data at fine spatial scales as scientists, land managers, and policy makers increasingly rely on spatially distributed simulation models to assess the effects of human activities on ecosystem services. Owing mainly to difficulties in extrapolating data collected from sparse networks of climate stations, high-resolution meteorological data are not available for many regions, especially for mountainous areas where the effects of terrain create spatially and temporally complex climatic patterns. This paper describes the development, application, and assessment of methods to construct daily high-resolution meteorological grids for the 2003 calendar year in the Upper South Santiam Watershed (USSW), a 500-km^2 mountainous catchment in the Cascade Range in western Oregon. Located within the Willamette National Forest, the USSW is managed pri-

Corresponding author address: Christopher Daly, PRISM Group, Department of Geosciences, 326 Strand Agriculture Hall, Oregon State University, Corvallis, OR 97331.
E-mail: daly@coas.oregonstate.edu

DOI: 10.1175/JAM2548.1

marily for forest products and wildlife habitat. The meteorological grids described here were developed to support a U.S. Environmental Protection Agency (EPA) modeling framework that combines a model simulating the effects of land use and climate on the structure of plant communities, which serve as wildlife habitat, with a spatially explicit model that simulates animal population responses to changes in habitat distribution and quality (Busing et al. 2007; McRae et al. 2006, manuscript submitted to *Ecol. Modell.*).

Meteorological elements modeled were minimum and maximum temperature; total precipitation, rainfall, and snowfall; and solar radiation and radiation-adjusted maximum temperature. The study area and digital elevation model (DEM) are discussed in section 2. Processing and quality control of station data are discussed in section 3. Section 4 presents methods for interpolating daily precipitation and temperature, and the separation of precipitation into rainfall and snowfall. Section 5 presents methods for modeling solar radiation. Section 6 discusses adjustments to daily maximum temperature to account for solar radiation exposure. Results and discussion are presented in section 7, and a summary and conclusions are presented in section 8.

2. Study area and digital elevation model

The USSW is located on the western slope of the Cascade Range, approximately 80 km east-northeast of Eugene, Oregon (Fig. 1). The watershed is approximately 508 km^2 in size, with elevations ranging from 1650 m at the headwaters region in the east to 194 m at Foster Lake, a reservoir that marks the lower terminus of the USSW in the west. The USSW is in the southeastern corner of the larger Santiam River Watershed, which encompasses 4737 km^2 of the eastern portion of the Willamette River basin and drains the Cascade Range.

The USSW is characterized by steep slopes and deeply incised drainages. Generally representative of the rugged mountainous landscape of the Pacific Northwest, the USSW contains representative examples of the region's conifer-dominated forest ecosystems. The species composition of forest communities is strongly associated with moisture and temperature gradients at different elevations (Franklin and Dyrness 1988).

The climate of the USSW is Mediterranean, characterized by copious winter precipitation and by summer drought; approximately 70%–75% of the annual precipitation falls during November–April. During winter, the polar jet stream steers a series of moist frontal systems from the Pacific Ocean onshore into the region. The USSW, located on the western, or windward, slopes of the Cascade Range, receives orographically enhanced precipitation that typically increases with elevation. Observed annual precipitation totals for 1971–2000 range from 1388 mm yr^{-1} at Foster Dam [Cooperative Observer Program (COOP) station 353047, 168 m; Fig. 1] to 2193 mm yr^{-1} at Jump Off Joe [snow telemetry (SNOTEL) station 22E07S, 1067 m; Fig. 1]. Temperatures are typically mild throughout the year, owing to the moderating influence of marine air from the Pacific Ocean, brought inland on persistent, onshore winds. The Cascade crest serves as an effective barrier to cold-air outbreaks originating in interior Canada to the northeast. Snow is relatively rare below about 500 m, but a substantial seasonal snowpack accumulates above about 900 m. Mean 1971–2000 January minimum temperatures at Foster Dam and Jump Off Joe are 1° and −2.6°C, respectively, and July maximum temperatures at Foster Dam and Jump Off Joe are 26.7° and 24.3°C, respectively.

Daily weather interpolation was performed on a 2-arc-s (~50 m) DEM in geographic (latitude/longitude) coordinates. The source for this DEM was the U.S. Geological Survey (USGS) 1-arc-s (~25 m) DEM (obtained online at http://gisdata.usgs.gov/NED/). A modified Gaussian filter (Barnes 1964) was applied to obtain 2-arc-s (~50 m) grid resolution (Fig. 1a). This 2-arc-s DEM was used to supply gridded elevations for modeling maximum and minimum temperature and solar radiation. For precipitation, the Gaussian filter (Barnes 1964) was applied to the 2-arc-s DEM to filter out terrain features up to 2.5 arc min (~4 km) in extent while retaining the 2-arc-s grid resolution (Fig. 1b). The direct effects of elevation on precipitation do not appear to be strong below scales of about 5–10 km, because of a number of mechanisms, including the advective nature of moisture-bearing airflow, the viscosity of the atmosphere, delays between initial uplift and subsequent rainout, and the movement of air around terrain obstacles (Daley 1991, 2006; Daly et al. 1994; Sharples et al. 2005). Larger-scale uplift seems to be especially characteristic of marine-based systems, such as those of western Oregon, because of the dominance of synoptic-scale storm systems over small-scale convective systems. To increase clarity, grid resolutions will hereinafter be given in approximate kilometers or meters, rather than geographic arc distances.

3. Station data

Daily data for maximum and minimum temperature, precipitation, and solar radiation for stations within the modeling region were obtained for the 2003 calendar year (Table 1; Fig. 1). Networks included the U.S. De-

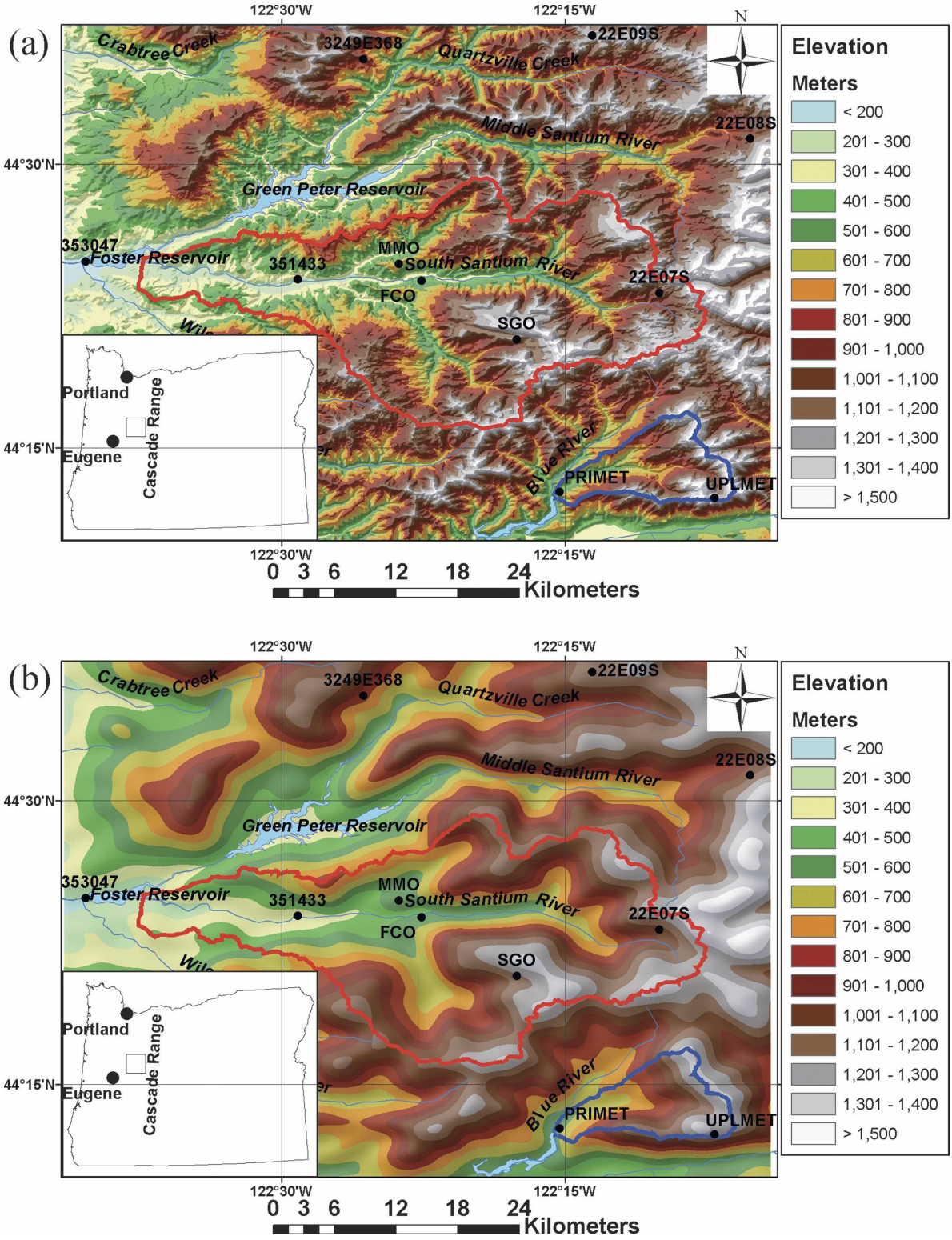

FIG. 1. The 2-arc-s DEM (a) used for temperature modeling and (b) low-pass filtered to a 2.5-arc-min effective wavelength for precipitation modeling. The USSW modeling area is outlined in red, and the HJA is outlined in blue. Locations of meteorological stations used in the analysis are shown as black dots.

TABLE 1. Stations in the USSW region and the observed meteorological elements used in this study. Here Tmin, Tmax, and Ppt are minimum temperature, maximum temperature, and precipitation, respectively.

Identification	Name	Elev (m)	Lon (°)	Lat (°)	Variables used	Network
22E07S	Jump Off Joe	1067	−122.1669	44.3861	Tmin, Tmax, Ppt	SNOTEL
22E08S	Daly Lake	1097	−122.0872	44.5219	Tmin, Tmax, Ppt	SNOTEL
22E09S	Little Meadow	1219	−122.2261	44.6131	Tmin, Tmax, Ppt	SNOTEL
3249E368	Yellowstone	939	−122.4278	44.5922	Tmin, Tmax	RAWS
351433	Cascadia	262	−122.4858	44.3981	Tmin, Tmax, Ppt	COOP
353047	Foster Dam	168	−122.6728	44.4139	Tmin, Tmax, Ppt	COOP
FCO	Falls Creek	534	−122.3764	44.3967	Tmin, Tmax, Ppt, PAR	EPA
MMO	Moose Mountain	668	−122.3967	44.4117	Tmin, Tmax, Ppt	EPA
SGO	Soapgrass	1206	−122.2928	44.3453	Tmin, Tmax, Ppt	EPA
TCO	Toad Creek	1202	−122.0378	44.4261	PAR, total radiation	EPA

partment of Agriculture (USDA) Natural Resources Conservation Service (NRCS) SNOTEL, the U.S. Department of Interior Remote Automatic Weather Station (RAWS), National Oceanic and Atmospheric Administration National Weather Service COOP, and EPA. Stations within the H. J. Andrews Experimental Forest (HJA) [primary meteorological (PRIMET) and Upper Lookout meteorological (UPLMET) stations] were not used directly in the modeling but were involved in the procedure to obtain radiation-adjusted maximum temperature. Toad Creek (TCO), used in the photosynthetically active radiation (PAR)–to–total radiation ratio calculations, is located about 8 km east of station 22E07S and is not shown in Fig. 1. For brevity and consistency, stations are hereinafter referred to by their identification string, which is given in the first column of Table 1.

All stations had a midnight-to-midnight daily observing period, except for the COOP sites 351433 and 353047. The observation time for these stations was 0800 local time. This circumstance required that the data be adjusted at these two stations to reflect better a midnight-to-midnight observing period. For temperature, the daily maximum was shifted back to the previous day and the minimum was left unchanged. For precipitation, two-thirds of the daily total was shifted back to the previous day and one-third was left unchanged. These adjustments assumed uniform weather conditions over the day; this assumption, while valid much of the time for temperature, was most likely violated on many days during the year for precipitation. There are some hourly precipitation data available for station 351433 from a different rain gauge and also from the EPA stations, but assimilating, quality controlling, and processing these data to apportion the daily precipitation values better was not within the scope of this project.

The daily station data were quality controlled (QC) in several ways. The EPA applied internal QC procedures to the EPA stations to ensure consistency of their data. Details of these QC procedures are documented and approved through a formalized quality assurance program at the EPA Western Ecology Division. In brief, these procedures included annual calibration checks of all climate sensors, quarterly or more frequent performance checks of station function, and QC of raw and summarized electronic data files. The RAWS, COOP, and SNOTEL networks all had internal QC procedures that assured at least a minimum acceptable level of data quality. However, additional QC checks were needed. Daily values of temperature and precipitation from all stations were aggregated to monthly values and mapped with the Parameter—Elevation Regressions on Independent Slopes Model (PRISM; see section 4) to assess if there were any chronic biases that could be identified at the monthly level that might be lost as noise at the daily level. No major problems were noted in the temperature data, but some serious precipitation issues were identified. As shown in Fig. 2, the observed December precipitation values at Moose Mountain (MMO) and Soapgrass (SGO) were very low when compared with precipitation at the other stations in the area. This discrepancy corresponded to a cold, snowy period between 20 November and 31 December during which the precipitation instrumentation did not collect precipitation effectively. The EPA precipitation gauges were unheated tipping buckets, which are susceptible to freezing and buildup of snow over the gauge orifice. Precipitation data from these two stations were therefore omitted from the analysis during this period. It is of interest that January and February, typically cold, snowy months, exhibited no appreciable precipitation undercatch, apparently because of warmer-than-normal temperatures that resulted in mostly rain at these stations. Although it is difficult to see in Fig. 2, precipitation data from the 22E07S (Jump Off Joe) SNOTEL site appeared to be low for September and October and were also omitted

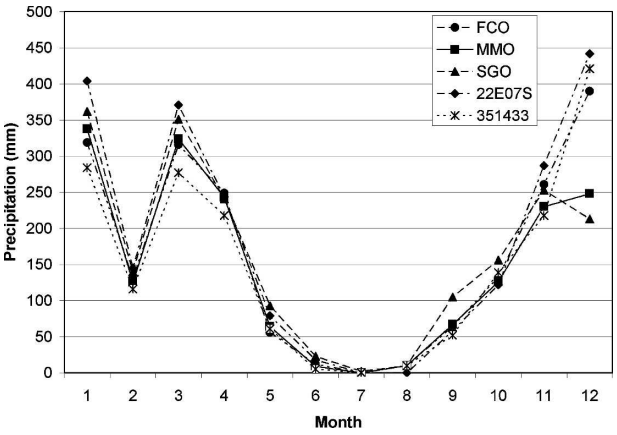

FIG. 2. Monthly total precipitation recorded during 2003 at the five stations located within the USSW.

from the analysis during this period. The reason for this discrepancy is unknown.

On the daily time step, a spatial quality control system currently in development for the USDA NRCS SNOTEL network (Daly et al. 2004) was applied to the temperature observations. The spatial QC system flagged spatially inconsistent or missing observations and replaced them with estimated values. Overall, 1% of the station days were missing. The station with the most missing data was MMO, with 21 missing days. Overall, 1% of the nonmissing values of maximum temperature were replaced with estimates. Station 3249E368 had the most replaced values, at 21. SGO had 11 values replaced; most occurred in January, and all appeared to be too high. Overall, 6% of the nonmissing values of minimum temperature were replaced with estimates. Again, station 3249E368 led, with 39 values replaced. SGO was second, with 32 values replaced; about one-half occurred in January, and all were flagged as being too high. Given the extreme spatial gradients in temperature caused by inversions, it is possible that some of the observations flagged as spatially inconsistent were in fact not erroneous.

Solar radiation observations were quality checked for reasonableness by comparing observed daily total radiation with modeled values (see section 4 and Fig. 5, described below). Solar radiation values at SGO and MMO showed considerable low biases in the spring (MMO) and autumn (SGO) that could not be readily explained. Therefore, radiation values at only Falls Creek (FCO) were used in the modeling study.

4. Temperature and precipitation modeling

Daily minimum and maximum temperature and total precipitation for the 2003 calendar year were interpolated using the PRISM system. An overview of PRISM and implementation of the model are described below.

a. PRISM overview

PRISM (Daly et al. 1994, 2002, 2003; Daly 2006) is often used to interpolate climate elements in a complex landscape like that of the USSW. The regression-based PRISM uses point data, a DEM, other spatial datasets, and an encoded knowledge base to generate repeatable estimates of annual, monthly, daily, and event-based climatic elements. These estimates are interpolated to a regular grid, making them compatible with GIS. Previous mapping efforts have included peer-reviewed, official USDA precipitation and temperature maps for all 50 states and the Pacific Islands; a new official climate atlas for the United States; a 110-yr series of monthly temperature, precipitation, and dewpoint maps for the conterminous 48 states; precipitation and temperature maps for Canada, China, and Mongolia; and the first comprehensive precipitation maps for the European Alps region (Daly et al. 2001; Hannaway et al. 2005; Milewska et al. 2005; Simpson et al. 2005). At the time of writing, reports and papers describing PRISM and associated spatial climate datasets are available online (http://prism.oregonstate.edu).

PRISM adopts the assumption that, for a localized region, elevation is the most important factor in the distribution of temperature and precipitation (Daly et al. 2002). PRISM calculates a linear climate–elevation relationship for each DEM grid cell, but the slope of this line changes locally with elevation as dictated by the data points. Beyond the lowest or highest station, the function can be extrapolated linearly as far as needed. A simple, rather than multiple, regression model was chosen because controlling and interpreting the complex relationships between multiple independent variables and climate is difficult. Instead, weighting of the data points (discussed later) controls the effects of variables other than elevation.

The climate–elevation regression is developed from x, y pairs of elevation and climate observations supplied by station data. A moving-window procedure is used to calculate a unique climate–elevation regression function for each grid cell. The simple linear regression has the form

$$Y = \beta_1 X + \beta_0, \tag{1}$$

where Y is the predicted climate element, β_1 and β_0 are the regression slope and intercept, respectively, and X is the DEM elevation at the target grid cell. The DEM elevation is represented at a spatial scale appropriate for the climate element being mapped (as discussed in section 2).

Upon entering the regression function, each station is assigned a weight that is based on several factors. In the general PRISM formulation, the combined weight of a station is a function of distance, elevation, cluster, vertical-layer, topographic-facet, coastal-proximity, topographic-position, and effective-terrain weights, respectively (Daly 2002; Daly et al. 2002). A subset of the PRISM weighting functions was used for the USSW application. Here, the combined weight W of a station was a function of the following variables:

$$W = f(W_d, W_z, W_c, W_l, W_t), \tag{2}$$

where W_d, W_z, W_c, W_l, and W_t are the distance, elevation, cluster, vertical-layer, and topographic-position weights, respectively. Distance, elevation, and cluster weighting are relatively straightforward in concept. A station is downweighted when it is relatively distant or at a much different elevation than the target grid cell or when it is clustered with other stations (which leads to overrepresentation; Daly et al. 2002).

The sheltered valleys of the USSW are highly susceptible to cold-air drainage and pooling. In the absence of solar heating or significant winds to mix the atmosphere, temperatures in these topographic situations stratify quickly, with cool, dense air draining into local valleys and depressions to form pools (Geiger 1965; Hocevar and Martsolf 1971; Bootsma 1976; Gustavsson et al. 1998; Lindkvist et al. 2000; Chung et al. 2006). This phenomenon results in temperature inversions, for which temperature increases rather than decreases, with elevation in a layer near the ground making a sharp transition to a more typical lapse rate above this layer (Clements et al. 2003). PRISM employs vertical-layer and topographic-position weighting to help to simulate these situations. In vertical-layer weighting, the meteorological stations entering the regression are divided into two vertical layers, and regressions are run on each separately. Layer 1 represents the boundary layer, and layer 2 represents the free atmosphere above it. A fuller discussion of the vertical-layer weighting function is available from Daly et al. (2002).

A useful way to assess a site's susceptibility to cold-air pooling is to determine its vertical position relative to local topographic features, such as valley bottom, midslope, or ridge top. (How this factor is implemented in PRISM has not yet been published and so is presented briefly here.) A "topographic index" grid was created that describes the height of a pixel relative to the surrounding terrain height. PRISM used this information to weight stations further during temperature interpolation. For the USSW application, an existing topographic-index grid created at 800-m resolution for nationwide modeling applications was filtered to 50-m resolution using a Gaussian filter (Barnes 1964). The 800-m topographic-index grid was developed through the following grid calculations: 1) starting with an 800-m DEM, the pixel with the lowest elevation within a 15-km radius is found; 2) the grid from step 1 is low-pass filtered to remove features of less than 15 km in horizontal extent using the Gaussian filter; and 3) subtract the grid from step 2 from the original 800-m DEM. The resulting grid represents the local, or relative, elevation variations within an approximate 15-km radius (Fig. 3). In this way, the effect of absolute elevation variations is minimized while local elevation variations are maximized (cf., e.g., Fig. 1a).

The selection of the 15-km search radius was a somewhat subjective and pragmatic one and depended largely on station data density. Cold-air drainage is a multiscale, fractal process, exhibiting patterns within patterns at scales ranging from large valleys that are tens of kilometers wide to narrow ravines of no more than a few meters in width. The density of station data dictates the scales that can be represented; the smaller the scale is, the denser is the network required. After some trial and error, it was determined that a 15-km radius seemed to represent the smallest scale that could be reasonably represented with routinely available station data.

Each station was assigned a topographic index according to its location on the topographic-index grid. Then, for each target grid cell (the pixel being modeled), the topographic-position weight for a station was calculated as

$$W_t = \begin{cases} 1 & \text{for} \quad \Delta t \le \Delta t_n \\ 0 & \text{for} \quad \Delta t > \Delta t_x \\ \dfrac{1}{\Delta t^z} & \text{for} \quad \Delta t_n < \Delta t < \Delta t_x \end{cases}, \tag{3}$$

where Δt is the absolute difference between the station and target-gridcell topographic index, z is the topographic-index-weighting exponent, and Δt_n and Δt_x are user-specified minimum and maximum topographic-index differences. If Δt for a station was less than or equal to Δt_n, the station received a full weight of 1. If Δt exceeded Δt_x, the station's weight became 0. For this application, the values of Δt_n and Δt_x were set to 100 and 500 m, respectively. The exponent z was set to 1.0, a value used in regions where cold-air-pooling effects are significant. Topographic-index weighting had the effect of increasing the weight of stations in the target grid cell's regression function that had topographic positions (and thus cold-air-drainage regimes) that were similar to the target grid cell.

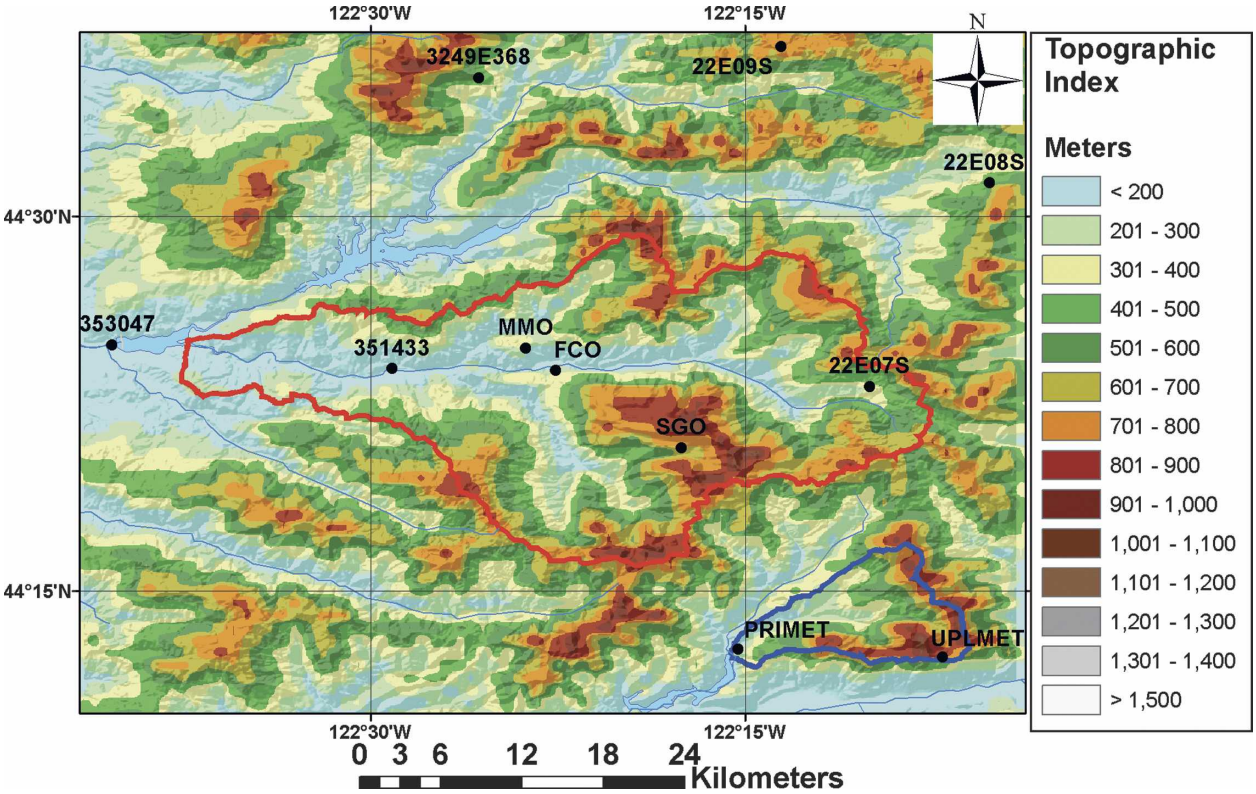

FIG. 3. The PRISM topographic-index grid for the USSW.

PRISM was parameterized by assessing general climatic patterns through use of the PRISM graphical interface and full grid applications at the monthly time step. A full discussion of all of the PRISM parameters is beyond the scope of this paper, but a detailed discussion of how PRISM is parameterized is given in Daly et al. (2002). Once an initial parameterization was determined, PRISM was run for all days in the year, and the resulting grids were evaluated for unusual conditions that were not handled well in the initial parameterization. This process was performed repeatedly until all days were modeled appropriately. Details for each climate variable are provided below.

b. Minimum and maximum temperature

It became clear early on that, for most of the year, the USSW was susceptible to strong minimum temperature inversions caused by cold-air drainage. Based on an analysis of the station data in the PRISM graphical user interface, the height of the inversion appeared to be relatively constant, at approximately 1000 ± 200 m. Therefore, when inversions occurred, 1000 m was set to be the dividing line between layers 1 and 2 in PRISM's two-layer atmosphere system, and stations within 200 m of this height were used in both layers (Daly et al. 2002). To determine if an inversion was occurring on a given day, PRISM compared the regression slopes in each layer, and if they were substantially different then an inversion was assumed and the 1000 ± 200 m dividing line was implemented. If the slopes were similar, the two layers were combined into one and a single regression function was calculated. Daily maximum temperature was also susceptible to inverted conditions, though not as frequently or strongly as minimum temperature. Therefore, PRISM was parameterized for maximum temperature in the same way as for minimum temperature, with the two-layer atmosphere (1000 ± 200 m potential inversion height) and with topographic-index weighting implemented. Further information and equations are available from Daly et al. (2002).

c. Precipitation

Daily precipitation was challenging to model, because of 1) the sometimes spotty nature of precipitation at small time steps, 2) the problems of inconsistent observing times between the COOP stations and the other networks, and 3) the difficulties of measuring snowfall, which can result in underreporting of precipitation and delays in measurement, that result from snow bridging and the freezing and subsequent thawing of the instru-

mentation. With these issues in mind, the approach to modeling precipitation was not to rely on daily data from any one gauge, but to try to simulate the larger-scale patterns that were present. This approach was consistent with the use of a DEM that was low-pass filtered to remove terrain features that were less than 4 km in size as the elevation input to the PRISM precipitation–elevation regression function. Given that precipitation patterns with wavelengths of less than 4 km were not to be simulated (see Fig. 1), PRISM was parameterized so that the minimum radius of influence was set to about 90 grid cells, or about 4 km. This meant that all stations within 4 km of the target grid cell would receive the same distance weight, thus producing a more generalized precipitation pattern.

d. Snowfall and rainfall

The gridded daily precipitation totals described above were separated into snowfall and rainfall components. The most important parameter determining precipitation form is the air temperature close to the ground, but it is also affected by the temperature profile above the ground, the characteristics of the precipitation particle, and the humidity of the air (Forland and Hanssen-Bauer 2000; Fuchs et al. 2001). The relationship between air temperature and the proportion of precipitation that fell as snow was investigated by analyzing daily data from the 22E07S SNOTEL station for 2003. SNOTEL stations include a snow pressure pillow for measuring the water equivalent of snow on the ground (SWE), a precipitation gauge for measuring total precipitation (liquid + solid), and an air temperature sensor. The daily ratio of snow accumulation to total precipitation data was calculated and was found to be very noisy, with many outliers, some with larger snow accumulations than total precipitation. This may have been caused by variations in snow-pillow response produced by melting and settling and by the coarse 2.54-mm precision of measured precipitation and SWE at SNOTEL sites. In general, however, the precipitation was nearly always snow at daily mean temperatures of −2.5°C and below and was nearly always rain at 4°C and above. Therefore, a linear regression function with these two temperatures as endpoints was used to estimate the proportion of daily precipitation as snowfall P_s:

$$P_s = -0.1667T_{m(\text{pixel})} + 0.6667, 0 \le P_s \le 1, \quad (4)$$

where $T_{m(\text{pixel})}$ is the daily mean temperature at each pixel in degrees Celsius. Each day, the total precipitation at each pixel was multiplied by P_s to obtain the daily snowfall, and rainfall was calculated as the difference between the total precipitation and the snowfall; $T_{m(\text{pixel})}$ was calculated as the average of the daily maximum and minimum temperatures. Maximum temperature unadjusted for the effects of solar radiation was used in the average (see section 6), because it was unlikely that solar radiation would have had an appreciable effect on precipitation form until it reached the ground. That said, solar radiation variations could have affected the melt rate of newly fallen snow, especially if it fell at temperatures near freezing.

Equation (4) gave a 50% snowfall–rainfall mix at a mean daily temperature of 1°C. This result corresponded well to Forland and Hanssen-Bauer's (2000) daily snow–rain threshold temperature of 2°C. Fuchs et al. (2001) reported a decrease in the 50% threshold temperature with increasing relative humidity, ranging from nearly 5°C at 50% relative humidity to about 0°C at 100% relative humidity. Given that the humidity during storms is relatively high within the USSW, a 50% threshold value of 1°C appeared reasonable.

5. Solar radiation modeling

The USDA Agricultural Research Service (ARS)–USGS version-2 version of the Image Processing Workbench (IPW) was used to perform many of the radiation calculations (Frew 1990; Marks et al. 1998). IPW is a UNIX-based portable image-processing program designed for hydrologic and biophysical modeling in addition to image analysis and remote sensing data processing. IPW produces topographically induced radiation grids that include the effects of elevation, slope, aspect, and shading and reflection from surrounding features. The effects of clouds on radiation were mapped outside the IPW system and inserted into the IPW radiation calculations (see section 5c).

IPW simulates solar radiation with a two-stream model that uses a multiple-scattering approximation of the radiative transfer equation to predict the scattering and absorption of light by the atmosphere (Dubayah et al. 1990; Dubayah 1994). The program operates under the assumption that, within the solar spectrum, a slope is irradiated from three sources—a direct beam from the sun, a diffuse beam from the sky, and direct and diffuse beams reflected by nearby terrain—and uses a relevant set of parameters that can be specified by the user (Dozier and Frew 1990). Single-scattering albedo and scattering asymmetry parameters are related to radiation extinction in the atmosphere (Dubayah et al. 1990). We used recommended values for these parameters of 0.8 and 0.6, respectively. A constant surface albedo of 0.15 was used over the entire modeling region, given that the region is heavily covered with co-

niferous forest, which has an albedo ranging from 0.05 to 0.20 (Oke 1987). No attempt was made to increase the surface albedo in certain areas and at certain times to account for the presence of snow on the ground. An optical depth value of 0.4 was used based on tests (described below) using observed solar radiation data.

Unless otherwise noted, the above values were used for all IPW calculations. Other parameters such as solar zenith angles and extraterrestrial radiation were based on solar geometry throughout the year and were calculated within IPW. Sky-view factors (percent of the sky visible) and terrain-configuration factors (geometric radiation effects between each pixel and other mutually visible pixels) were calculated within IPW from the DEM.

The five steps taken to map daily solar radiation for 2003 over the USSW are summarized as follows:

1) Simultaneous measurements of PAR and total solar radiation at station TCO were used to calculate a conversion factor to estimate total solar radiation from PAR.
2) IPW software was used to map potential "clear sky" solar radiation each day.
3) PAR data from station FCO and the total solar radiation conversion factor obtained in step 1 were used to calculate the ratio of observed daily solar radiation to the estimated clear-sky radiation from step 2; this ratio is referred to as the "cloud factor."
4) The cloud-factor grids from step 3 were used to calculate the approximate ratio of direct to diffuse radiation at each pixel, following the method of Bristow and Campbell (1985).
5) The IPW software, with the cloud factor grids from step 3 and the direct/diffuse ratio grids from step 4 as inputs, was used to map total solar radiation.

Each step is described in more detail below.

a. Converting PAR to total solar radiation

Solar radiation observations at FCO were of PAR, but total radiation was required for compatibility with the IPW calculations and to model maximum temperature adjustments (discussed later). There were observations of both PAR and total radiation at TCO, about 8 km east of station 22E07S, which allowed for a comparison of the two radiation measurements. As shown in Fig. 4 below, the hourly total radiation (MJ m^{-2}) was, on average, 1.8288 times the PAR flux (μmol m^{-2} s^{-1}). This compares reasonably well to, but is somewhat lower than, a multiplier of 2.0699 calculated by Ting and Giacomelli (1987). Using the locally derived 1.8288 multiplier produced much better results than the 2.0699 multiplier when comparing total radiation estimates with clear-sky estimates from the IPW calculations, and so it was adopted for all sites.

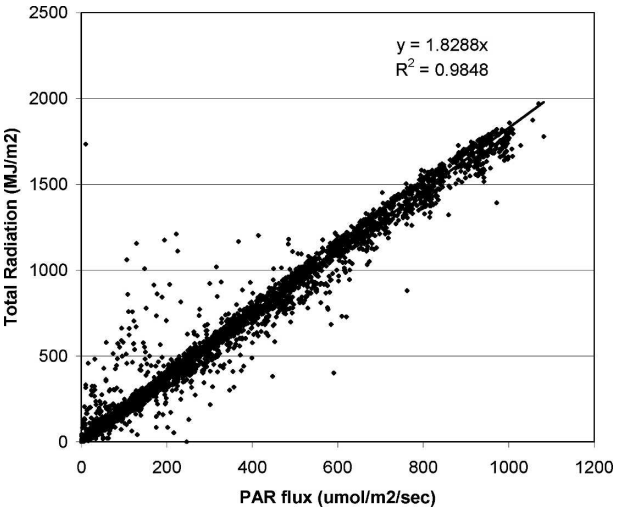

FIG. 4. Scatterplot and linear regression function of total solar radiation vs PAR at TCO.

b. Mapping clear-sky radiation

The next step in the process was to calculate direct and diffuse clear-sky radiation over the study area for each day. This is the potential radiation that would be received if the sky was free of clouds and other local attenuating effects such as air pollution. The direct beam at each pixel was attenuated by multiplying the incoming value by a horizon mask, calculated with solar geometry.

IPW was first used to calculate exoatmospheric radiation, which is the radiation received at the top of the atmosphere (an elevation of 40 000 m was used). The effects of elevation on both direct and diffuse radiation were then accounted for by using the DEM and invoking atmospheric density attenuation within IPW. The direct and diffuse components were combined to give clear-sky radiation values at each pixel, treating them as horizontal surfaces. Horizontal surfaces were modeled here because radiometers typically measure radiation over a hemisphere leveled horizontally.

Because IPW radiation calculations are sensitive to of specifications optical depth t, care was taken to determine the optimal value to use. Daily solar radiation data from FCO were plotted against IPW's clear-sky estimates using various values of t. Visual comparison between the observed clear-sky envelopes (generally the highest daily radiation values at a given time of year) and IPW's theoretical curves revealed the optimal value of t to be approximately 0.4 (Fig. 5). With $t = 0.4$, IPW-predicted clear-sky radiation matched clear-sky

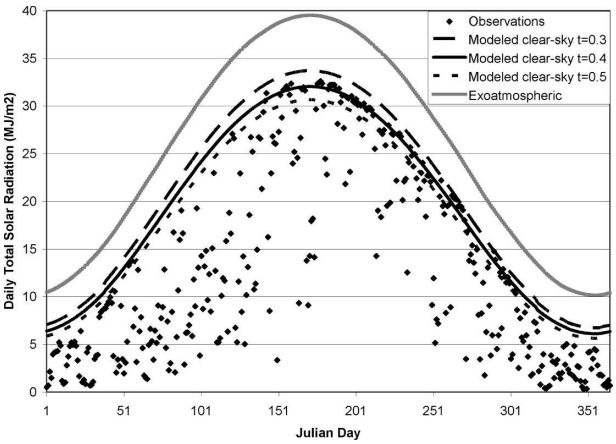

FIG. 5. Observed 2003 daily total solar radiation (estimated from PAR), and modeled clear-sky and exoatmospheric radiation for FCO. Modeled clear-sky radiation is shown for three optical depth values: $t = 0.3$, 0.4, and 0.5. A t of 0.4 was found to be the optimal value.

observations reasonably well. IPW clear-sky algorithms were run on each day at 1-h intervals, with the 1-h radiation values summed to obtain daily totals for each day. Tests were conducted to determine if a more computing-intensive 20-min calculation interval would produce better results, but differences between daily total solar radiation values calculated at 1-h and 20-min intervals were insignificant.

c. Mapping cloud factor

A daily cloud factor was calculated for each station by dividing the observed daily total solar radiation at FCO by IPW's theoretical clear-sky values at this same location. In essence, the cloud factor represented the proportion of the potential clear-sky radiation that was recorded by the measuring instrument. As such, it is not just a cloud factor, because it takes into account other attenuating factors, such as dust, haze, and air pollution, as well as objects that may be blocking or reflecting radiation, such as buildings or vegetation. Because the daily cloud factors were derived from one station within the USSW, the implicit assumption was that the daily cloud factor was constant across the USSW.

d. Calculating direct/diffuse ratio

Separate calculation of the direct and diffuse fractions of total radiation is desirable because as they change, the effect of topography on total radiation changes. For example, on a cloudy day when the fraction of diffuse radiation is high, the light will appear "flat," with relatively small radiation differences between a slope facing toward the sun and one facing away. Conversely, on sunny days when the fraction of diffuse radiation is low, slopes facing toward and away from the sun will exhibit sharply different radiation regimes, due in large measure to the large difference in direct-beam radiation received. In this study, direct and diffuse fractions were calculated and entered into IPW separately, allowing it to evaluate topographic effects explicitly.

Bristow and Campbell's (1985) equation was used for determining the percentage of diffuse radiation from total radiation. This equation requires a value of T_t, the total transmittance on a horizontal surface. The T_t is slightly different from the cloud factor, in that it is the ratio of the observed to the potential exoatmospheric radiation (at 40 000 m) rather than the ratio of the observed to the potential clear-sky radiation at the elevation of the station. The T_t was calculated by multiplying the daily clear-sky radiation grids by the cloud factor grids to obtain daily horizontal-surface cloud-adjusted radiation grids. Dividing these grids by IPW's computed extraterrestrial (potential) radiation grids gave daily "transmittance coefficients" for each pixel.

The general form of the Bristow–Campbell equation is

$$T_d = T_t\{1 - \exp[0.6(1 - B/T_t)/(B - 0.4)]\}, \quad (5)$$

where T_t is daily total transmittance on a horizontal surface, T_d is daily diffuse transmittance on a horizontal surface, and B is maximum clear-sky transmissivity (Bristow and Campbell 1985). We used $B = 1.0$, a value used in northwestern U.S. regional studies, giving the simplified Bristow–Campbell equation

$$T_d = T_t[1 - \exp(1 - 1/T_t)]. \quad (6)$$

e. Final mapping of solar radiation

In the final step, the cloud-adjusted horizontal surface radiation grids were multiplied by the appropriate diffuse and direct proportions and IPW was used to calculate topographically sensitive radiation across the study area. The resulting radiation grids accounted for cloudiness, proportions of direct and diffuse radiation, terrain shading and reflection, and slope/aspect/elevation effects for each day. The final radiation values for each pixel were calculated assuming their surfaces to be sloped according to the DEM and not to the value a leveled radiometer would record.

6. Radiation-adjusted maximum temperature modeling

Slope and aspect modulate near-surface daily maximum temperatures based on exposure to solar radiation and wind (McCutchan and Fox 1986; Barry 1992;

Bolstad et al. 1998; Lookingbill and Urban 2003). The gridded daily maximum temperatures described previously in this paper represent temperatures at approximately 1.5–2 m above ground in generally flat and open conditions (i.e., conditions at the measurement sites). In this study, maximum temperature values were adjusted for the effects of differing solar radiation exposure. Adjustments were made based on results from a temperature study performed in the HJA, located in an adjacent watershed to the south of the USSW (Fig. 1; Smith 2002). In this study, 1971–2000 mean monthly maximum temperatures at approximately 2 m above ground were compared at pairs of sites with varying degrees of solar radiation attenuation caused by terrain shading and canopy cover. Seven site pairs were selected to develop the relationships. Pair members had to be within 50 m in elevation of one another and both had to be physically located within the boundaries of the HJA (approximately 10 km $\times$ 12 km in size) to minimize elevation or regional biases. No sites near streams were used, because of the localized cooling effects of running water and cold-air drainage. Other factors deemed capable of creating local biases, for example, forest-edge effects, eliminated sites from consideration (Smith 2002).

The IPW-based method described above was used to estimate cloud-adjusted radiation at each site (Smith 2002). Solar radiation observations from UPLMET were used to determine representative cloud factors for the sites that made up the nine pairs. UPLMET is one of five benchmark meteorological stations within the HJA and is located at 1292 m MSL in the southeastern portion of the forest (Fig. 1). Solar radiation data from UPLMET alone were used because the site is largely flat and open, and the data are of high quality. UPLMET data were used to develop cloud factors for the HJA in a similar way that FCO data were used to determine cloud factors for the USSW, except that the daily UPLMET data were first averaged monthly over the period 1995–2000 (period of available data).

To quantify the effects of the terrain blockage and forest canopy on each site's radiation regime, hemispherical "fish eye" photographs were taken at each site and analyzed. Most photos were taken in the autumn, when deciduous trees were in the process of losing their leaves. Seasonal effects on canopies were minimal at these sites, because the canopies were predominantly evergreen needleleaf. Such photography has long been used in forest research and is an effective tool for characterizing forest light regimes (Chan et al. 1986; Vales and Bunnell 1988; Easter and Spies 1994). HemiView software (Delta-T Devices 1999) was used to analyze the fish-eye photographs for blockage of direct and diffuse radiation [see Smith (2002) for details].

TABLE 2. Slope of linear regression function for 1971–2000 mean daily maximum temperature difference (°C) vs site-pair solar radiation difference (MJ m^{-2}) in the HJA. HJA radiation shields were used at all sites (see text). Solar radiation was estimated at each site with IPW and hemispherical photographs. Seven site pairs were used.

Month	Regression slope [°C MJ^{-1} $(m^2$ day$)^{-1}$]	R^2
Jan	1.17	0.91
Feb	0.73	0.96
Mar	0.45	0.96
Apr	0.33	0.99
May	0.24	0.82
Jun	0.22	0.84
Jul	0.20	0.74
Aug	0.25	0.82
Sep	0.34	0.87
Oct	0.52	0.91
Nov	0.76	0.92
Dec	1.41	0.95

Monthly linear regression relationships were developed between site differences in modeled solar radiation exposure and differences in 1971–2000 mean maximum temperature (Table 2). Seasonal effects were immediately apparent. During the winter months when radiation levels were low, regression slopes were greatest. During the months of maximum radiation, slopes were relatively low. Thus, a megajoule per meter squared·per day radiation difference had a much greater effect on maximum temperatures in low-radiation conditions than in high-radiation conditions. Overall, a 50% change in radiation resulted in a 2°–3°C change in mean monthly maximum temperature. This was similar to 2°–3°C differences observed by Running and Nemani (1985) between north- and south-facing slopes in Montana.

Although the slopes in Table 2 were derived from 30-yr monthly averages, the same general relationships were expected to be applicable for use on a daily basis. However, doing so required that the varying slope of the linear regression function be generalized for daily-varying radiation conditions. This was done by developing a relationship between the regression slope and 1995–2000 mean monthly solar radiation at UPLMET. Hemispherical photography and IPW radiation modeling methods used to estimate radiation at the seven site pairs were used to remove the effects of canopy and horizon shading on UPLMET observed radiation, thus creating "flat and open" radiation estimates at the site. Modeled flat-and-open radiation values were available for both HJA and the USSW from the IPW calcula-

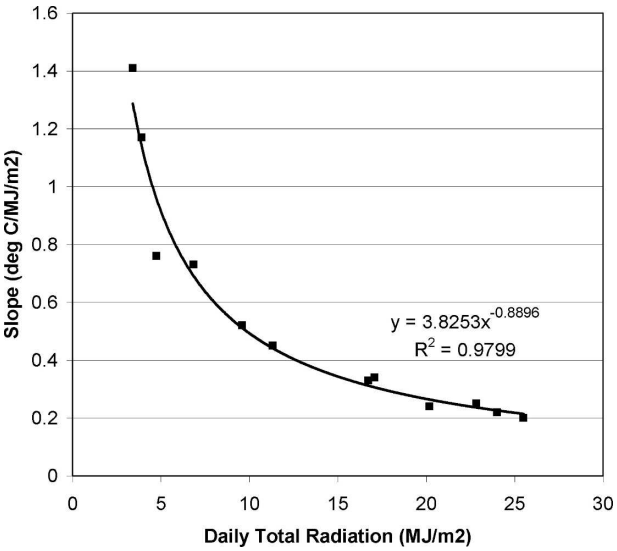

FIG. 6. Power-law function describing the relationship between the slope of the linear regression function relating site-pair solar radiation difference (MJ m^{-2}) to 1971–2000 mean daily maximum temperature difference and 1995–2000 mean monthly total daily solar radiation at UPLMET. Solar radiation has been adjusted to remove the effects of canopy and horizon shading.

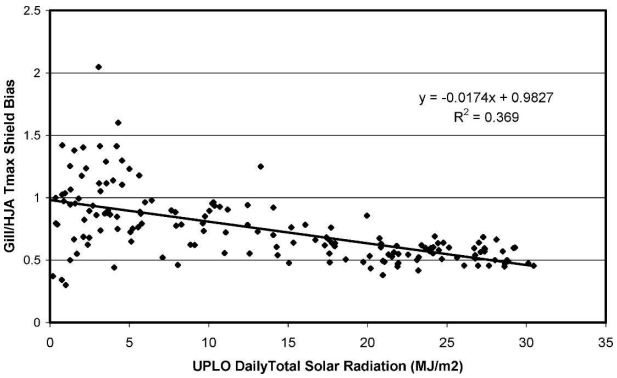

FIG. 7. Relationship between ratio of Gill to HJA shield daily maximum temperature bias [(Gill − aspirated)/(HJA − aspirated)] and daily total solar radiation observed at UPLMET for 7 Jul–31 Dec 2003.

tions, allowing the relationship to be transferred to the USSW. The relationship was fitted with a power-law function:

$$M = 3.8253R_{e(\mathrm{UPLMET})}^{-0.8896}, \quad (7)$$

where M is the slope of the linear regression function and $R_{e(\mathrm{UPLMET})}$ is UPLMET radiation adjusted to remove the effects of canopy and horizon shading (Fig. 6). UPLMET began operation in 1995, and thus the observation record is relatively short. However, given the strength of the derived relationship it is unlikely that the differences in averaging period would have affected the results appreciably.

The temperature stations used in Smith's (2002) study employed a nonstandard radiation shield called an "HJA shield," which consisted of a polyvinyl chloride pipe cut in half lengthwise, placed over the top of the temperature sensor (concave side down), and oriented in a north–south direction. In contrast, most temperature sensors today, including those within the USSW, are fitted with cylindrical Gill-type shields or a similar device. This limited the applicability of the relationships discussed above. To gain information on how the HJA shield compared to the more commonly used Gill shield, a side-by-side comparison was done for 7 July–31 December 2003. An aspirated temperature sensor (used as the control) was placed next to an HJA shield and a Gill shield at 1.5 m above ground at PRIMET (442 m MSL), within the HJA and approximately 10 km west of UPLMET (Fig. 1). Daily maximum temperatures were recorded for the three shields, and differences between the Gill and HJA shields and the aspirated control were calculated.

Temperature biases caused by radiation shields are influenced primarily by wind speed and solar radiation (Anderson and Baumgartner 1998; Hubbard et al. 2004). However, utility in the USSW study, where wind speed was not estimated, required that a relationship with solar radiation only be attempted. A formula to convert from HJA shield temperatures to Gill temperatures was found by regressing the ratio of the Gill shield bias to the HJA shield bias against UPLMET daily total solar radiation (Fig. 7). It was beyond the scope of this study to adjust the UPLMET daily radiation observations for the effects of canopy and horizon shading, but the effects would have been very minor. Five days for which the HJA and Gill biases were of different sign (typically low-radiation days when the biases were small) were omitted from the dataset for this analysis. A linear regression function resulted that predicted a ratio of near 1.0 (no difference) on low-radiation days to about 0.5 on high-radiation days (Gill bias = 0.5 × HJA bias):

$$C = 0.0174R_{t(\mathrm{UPLMET})} + 0.9827, \quad (8)$$

where C is the HJA-to-Gill shield correction factor and $R_{t(\mathrm{UPLMET})}$ is the daily total solar radiation observed at UPLMET.

The final equation used to adjust daily maximum temperature in the USSW for the effects of solar radiation variation was then

$$T_{\mathrm{xr(pixel)}} = T_{x(\mathrm{pixel})} + MC[R_{t(\mathrm{pixel})} - R_{e(\mathrm{pixel})}], \quad (9)$$

TABLE 3. Jackknife cross-validation error statistics for the interpolation of daily maximum and minimum temperature and precipitation, summarized by month. Results are for the five stations within the USSW: 351433, FCO, MMO, SGO, and 22F07S.

	Max temperature (°C)		Min temperature (°C)		Precipitation (mm)		Precipitation (%)	
Month	Bias	MAE	Bias	MAE	Bias	MAE	Bias	MAE
Jan	−0.15	0.89	−0.30	0.86	0.73	2.05	6.62	18.62
Feb	0.04	0.55	−0.22	0.83	0.29	1.71	5.95	35.03
Mar	−0.09	0.50	−0.10	0.57	1.07	3.47	10.10	32.83
Apr	0.07	0.43	−0.10	0.40	0.10	2.16	1.32	27.11
May	−0.12	0.50	−0.22	0.69	0.09	1.28	3.85	56.54
Jun	−0.09	0.59	−0.28	0.89	0.06	0.42	13.07	96.00
Jul	−0.20	0.64	−0.42	1.36	−0.01	0.02	−43.18	156.82
Aug	−0.33	0.75	−0.35	1.09	−0.04	0.14	−10.96	43.72
Sep	−0.22	0.64	−0.33	1.12	−0.08	0.96	−3.52	39.84
Oct	−0.16	0.68	−0.28	0.98	0.09	1.27	2.03	28.64
Nov	−0.10	0.60	−0.33	0.87	−0.09	2.07	−1.22	27.80
Dec	−0.02	0.66	−0.22	0.67	−0.14	2.99	−1.11	24.30
Annual	−0.12	0.62	−0.26	0.86	0.20	1.51	3.97	29.30

where $T_{xr(\text{pixel})}$ is the adjusted maximum daily temperature at each pixel, $T_{x(\text{pixel})}$ is the unadjusted (original) daily maximum daily temperature, $R_{t(\text{pixel})}$ is the IPW-modeled solar radiation at each pixel accounting for the effects of slope, aspect, and horizon shading, and $R_{e(\text{pixel})}$ is the IPW-modeled flat-and-open solar radiation at each pixel.

7. Results and discussion

a. Minimum and maximum temperature

Daily minimum temperatures were dominated by the restrictive terrain of the USSW, which allowed cold-air drainage and promoted the formation of inversions in most seasons. The only season to show relatively weak minimum temperature inversions was spring, when the atmosphere was relatively well mixed. The two-layer-atmosphere and topographic-index weighting functions in PRISM were used in the station-weighting process to help to simulate what were often sharply defined inversions. On most days with inversions, the coldest air settled along the South Santiam River near station 351433, which is relatively low and is bordered by steep slopes. On days with the most-well-developed inversions, the minimum temperature difference between 351433 and MMO and SGO (400–600 m higher on the ridges above) was as much as 10°–13°C.

As was expected, maximum temperature exhibited fewer instances of inversions, because of daytime solar heating. Most inversions occurred during the low-sun months of November–January. During these months, a lack of solar radiation, surface heating, and ventilation often allowed inversions to persist all day.

Table 3 summarizes PRISM jackknife cross-validation bias (predicted − observed) and mean absolute error (MAE; |predicted − observed|) of daily minimum and maximum temperature for the five stations within the USSW, averaged for each month. In jackknife cross validation, each station was omitted from the dataset, predicted in its absence, and then returned to the dataset. The prediction bias indicates the tendency for PRISM to overpredict (positive bias) or underpredict (negative bias). The MAE indicates how far, on average, the prediction was from the observation. Cross-validation statistics are not given for radiation-adjusted maximum temperature, because the adjustment is a postprocessing step after interpolation has occurred. Moreover, there were no temperature observations in areas of significant slope that could be used for evaluation.

Overall, prediction bias was generally less than 0.5°C, and MAE was less than 1°C. Errors for minimum temperature were greater than those for maximum temperature, owing to the more complex relationship between minimum temperature and topography. Figure 8 illustrates monthly trends in the prediction bias of daily minimum temperature for each station within the USSW. Stations 351433 and 22E07S were predicted with the least bias. This was probably due to the presence of stations outside the USSW with similar elevations and topographic positions. Prediction biases of the three EPA stations varied by season and topographic position. SGO and MMO, which are ridge-top stations, were consistently underpredicted, especially in summer. This was a result of their very warm minimum temperatures near the top of the persistent inversion. FCO, located deep in the Santiam River Valley, was overpredicted in summer, likely because of its small horizontal distance from MMO. These results suggest that SGO, MMO, and FCO, though just a few kilome-

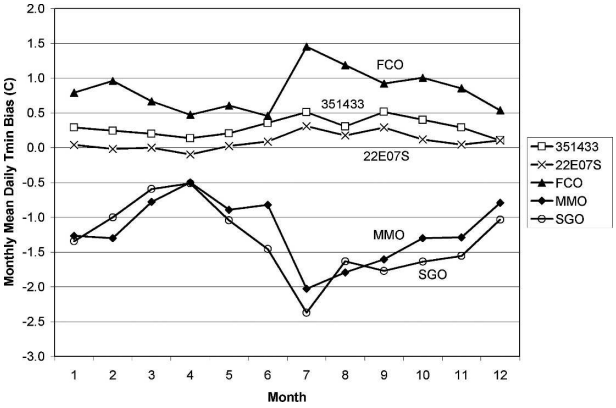

FIG. 8. PRISM bias (predicted − observed) of daily minimum temperature for each station within the USSW, averaged for each month in 2003.

ters apart, represented very different temperature regimes, dictated by cold-air drainage and temperature inversions in both winter and summer, and thus "competed" with each other in the jackknife cross-validation process.

Competition between SGO and MMO was further illustrated in a sensitivity study for which the interpolation bias in minimum temperature estimation was calculated at SGO and MMO for four different inversion height parameterizations in PRISM: 500, 750, 1000, and 1250 m (Fig. 9). An inversion height at 1250 m effectively represented a noninversion (one layer) parameterization, because all stations were located below this elevation. The smallest bias at MMO was achieved with a 750-m inversion height, and the smallest bias at SGO occurred with a 1000-m inversion height. These differences are difficult to attribute, but may be caused by sensor siting, slope, and topographic positions, and other highly local conditions. Interpolation bias was least sensitive to inversion height in spring, when the atmosphere was relatively well mixed, and was most sensitive in summer, when inversions occurred nearly every night. Although there may be some inconsistencies in the station observations that bear further investigation, it is clear that without these stations the interpolated grids would have been less successful in delineating these sharp temperature gradients. It is likely that additional data at various levels above the river in other parts of the USSW would have resulted in further improvements to the grids.

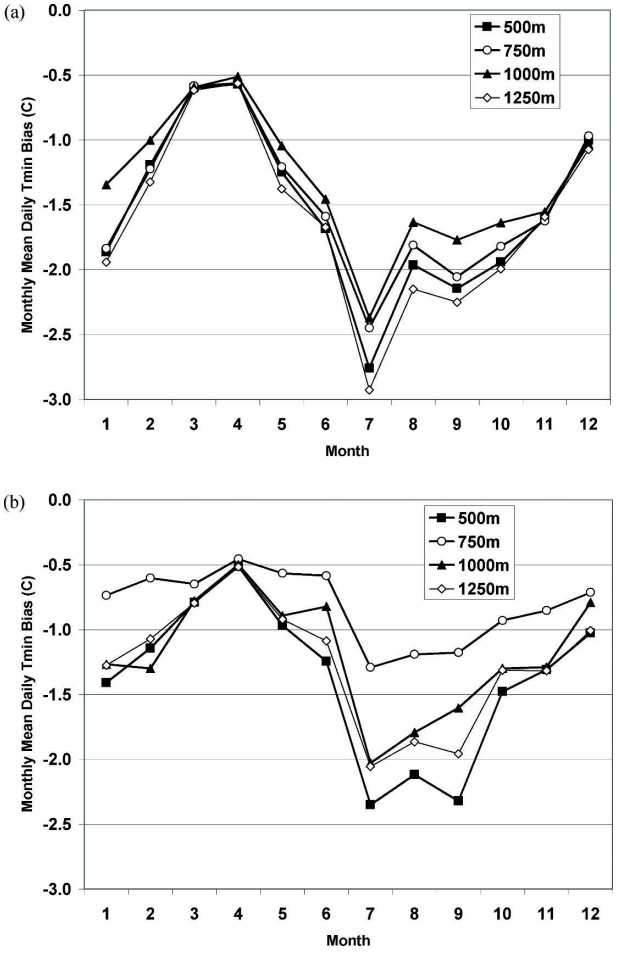

FIG. 9. PRISM bias (predicted − observed) of daily minimum temperature for stations (a) SGO and (b) MMO at four different inversion-height parameterizations ranging from 500 to 1250 m, averaged for each month in 2003.

b. Precipitation, snowfall, and rainfall

Precipitation typically increased with elevation in the USSW, increasing by about 50% per kilometer of elevation. However, several days exhibited conditions that were wetter over the lower elevations of the watershed than over the higher elevations. This effect could have been caused by three factors: 1) the daily precipitation values were a "snapshot" of a storm that was working its way up the valley, eventually covering the entire watershed; 2) storms that have a shallow moisture source could produce effects similar to those of a shallow marine layer, which does not penetrate very deeply into the Cascades; and 3) there may have been less-than-perfect time shifting and apportioning of daily precipitation at the low-elevation COOP sites. The time-shifting problem was probably the cause of local maxima or minima in the daily precipitation fields that occurred occasionally around station 351433. Discrepancies were often seen around other stations as well, which could have been caused by natural spottiness in the precipitation field, delays in the recording of precipitation that were due to snowfall buildup and

TABLE 4. Observed and predicted precipitation frequency statistics for stations within the USSW for 2003. Predicted values are taken from the grid cell containing the station location.

Station	Days ≥1 mm	Days ≥10 mm	Days ≥25 mm	Days ≥50 mm
22E07S				
Observed	163	76	28	3
Interpolated	188	71	26	3
351433				
Observed	183	61	12	1
Interpolated	178	61	15	1
FCO				
Observed	158	70	19	2
Interpolated	164	67	17	2
MMO				
Observed	149	63	17	2
Interpolated	166	69	17	2
SGO				
Observed	155	71	19	2
Interpolated	182	85	25	2

subsequent melting or falling into the gauge, or errors in data processing.

Jackknife cross-validation errors for daily precipitation are summarized by month in Table 3. Daily precipitation totals were highly variable, and interpolation errors were similarly so. Table 3 gives errors in both absolute (mm) and relative (%) terms. Bias was generally about 1 mm or less, and MAE was less than 4 mm day^{-1}. These values constitute a highly variable percentage of the daily totals, owing to the summer-dry/winter-wet climate of the USSW (see Fig. 2). In the wet months of November–April, the MAE was about 20%–30% of the daily precipitation. In the drier months, the MAE was greater than 50%, and was as high as 150% in July. However, in absolute terms, the July MAE was only 0.02 mm.

In addition to total amounts, it is useful to evaluate how well the interpolation procedure reproduced observed daily precipitation frequencies (Thornton et al. 1997). Table 4 shows observed and interpolated frequencies of daily precipitation at four intensities: 1, 10, 25, and 50 mm. Observed and interpolated precipitation frequencies were very close for all intensities at the rain-dominated stations 351433 and FCO. For the higher-elevation stations, the interpolated frequency of days with at least 1 mm of precipitation was about 10%–12% greater than that observed. This appears to have been caused by two factors. First, because of underreporting problems, data from SGO and MMO were not used between 20 November and 31 December, and data from 22E07S were not used in September and October; thus, the observed frequency was probably too low at these stations. Second, because of discrepancies in the timing of measured daily precipitation across the upper elevations, and given the broad physical patterns of precipitation, PRISM was parameterized so that the minimum radius of influence was set to about 4 km, thus producing a more generalized precipitation pattern that occasionally produced small amounts of precipitation in regions where none was observed.

A notable feature of Table 4 is the relatively large number of days on which at least 1 mm of precipitation was observed at station 351433. As discussed in section 3, the procedure for estimating midnight-to-midnight precipitation at COOP stations observing at 0800 local time was to shift two-thirds of the daily total back to the previous day and leave one-third unchanged. This procedure has the effect of artificially increasing the number of days with precipitation, especially light amounts. In future work, a more suitable procedure might be to shift the entire precipitation amount to the previous day. This method would introduce some additional error into the timing of the precipitation, which could increase spatial discontinuities in the precipitation fields, but would maintain the frequency of daily precipitation intensities. Tests showed that this method reduced the number of days with at least 1 mm of precipitation at station 351433 from the current 183 to 157, which is more in line with the other stations.

The range of temperatures experienced in the USSW during storms encompassed the 1°C 50% rain/snow value [Eq. (4)] during most events. The lowest elevations received nearly all precipitation in the form of rain while higher elevations received both rain and snow. As a reasonableness check of Eq. (4), daily interpolated rainfall and snowfall were summed to annual totals for the pixel containing the SNOTEL station 22E07S, which operated a snow pillow. The interpolated values showed that 40% of the annual precipitation fell as snow in 2003. This matched the observed snowfall percentage of 22E07S perfectly, suggesting that the simple linear temperature model for estimating the snowfall/precipitation proportion functioned well at this location.

c. *Solar radiation and radiation-adjusted maximum temperature*

Solar radiation was modulated considerably by the deeply divided terrain of the USSW. The greatest spatial variation occurred on sunny days, when the proportion of direct radiation was greatest. On such days, sheltered, north-facing slopes received less than one-third of the total daily solar radiation received by flat-and-open locations. The greatest absolute variation among slopes occurred on sunny days during the spring and

late summer, when radiation received was reasonably high, but the sun did not rise and set in the northeast and northwest, respectively, which illuminated north-facing slopes during early and midsummer. The greatest percent variation among slopes occurred on sunny days during winter, when the sun was low and radiation received was also low.

Radiation effects, as modeled for daily maximum temperature, were important on sunny days, but were of little consequence on cloudy days. On sunny days, daily maximum temperatures in deeply shaded areas were simulated to be up to 3°–4°C cooler than those in flat-and-open areas. The net result of including solar radiation effects on temperature was to lower the overall basin-average daily maximum temperature slightly, because the available temperature data were typically observed in flat-and-open-terrain locations, which received relatively high solar radiation totals.

Insufficient data were available with which to perform quantitative error analyses for solar radiation and its effects on radiation-adjusted daily maximum temperature, but there were several sources of error nonetheless. These included 1) the DEM, 2) measurements of PAR, 3) conversion of PAR to total solar radiation, 4) use of measurements at a single station to represent the USSW, 5) simulation of solar radiation with IPW, and 6) estimation of the effects of changes in solar radiation exposure on daily maximum temperature. DEM error, which was a source of uncertainty in temperature and precipitation interpolation, most likely had the greatest impact on solar radiation calculations because of the sensitivity of the radiation calculations to not only elevation, but also local slope, aspect, and shading terrain features. Additional error was introduced by filtering the 25-m DEM to 50-m resolution, which reduced its effectiveness at resolving small terrain features and led to altering simulated radiation exposure in some locations.

As has been discussed in this paper, the relationship between PAR and total solar radiation was estimated for the USSW based on measurements of both quantities at one station (TCO) outside the USSW. However, given the strength of the relationship ($R^2 = 0.98$, where R is correlation coefficient) and the similarity in environmental conditions between TCO and the USSW, this was likely not an important source of error. Because of difficulties with solar radiation measurements at two out of three stations within the USSW, radiation from only one station (FCO) was used to represent the entire USSW. Although FCO was subject to its own set of exposure, topographic position, and canopy effects, the good correspondence between observed radiation and IPW-simulated radiation gives us confidence that the observed and estimated radiation are reasonable.

The regression equations used to estimate the effects of changes in solar radiation exposure on daily maximum temperature were developed in nearby HJA, but two problems had to be overcome: 1) temperature measurements were taken with "HJA" shields and not from Gill-type shields and 2) the equations were developed from long-term monthly mean maximum daily temperatures and not from individual daily temperatures. The radiation shield comparison revealed a maximum difference between the shields of about 1°C that could be partly explained by solar radiation exposure; therefore, the shield discrepancy contributed less than 1°C to the adjustment error. The relationships developed between solar radiation and the slope of the regression function relating maximum temperature change with solar radiation change were very strong ($R^2 = 0.98$), suggesting that the use of long-term monthly equations for daily temperatures did not introduce large errors into the calculations.

d. Example daily meteorological grids

Figures 10–14 show examples of the daily meteorological grids developed for the USSW. Figure 10 shows USSW daily meteorological grids for 17 February 2003. A storm produced significant precipitation on this day, primarily rain at lower elevations and snow at higher elevations. The diurnal temperature range (TMAX − TMIN, defined in Fig. 10 caption) and differences between radiation- and nonradiation-adjusted maximum temperatures were minimal, because of the cloudy weather, as evidenced by low solar radiation.

Figure 11 shows daily meteorological grids for 19 June 2003. Despite being near the summer solstice, solar radiation conditions caused by clouds and rain were similar to those that would be expected during the winter season. "Flat" light conditions (i.e., high diffuse component) produced relatively small topographic differences in solar radiation, and thus differences between radiation-adjusted and -unadjusted maximum temperatures were also small.

Figure 12 shows daily meteorological grids for 29 July 2003. This date was one of the warmest days of the year, and temperatures exceeded 34°C almost everywhere. Minimum temperatures were strongly inverted on this stable, summer day. Remnants of the morning inversion appeared to be present at middle elevations, producing a relatively cool zone just above the river. Solar radiation was very high, except for highly sheltered, north-facing slopes.

Figure 13 shows daily meteorological grids for 4 October 2003. This day was dry and stable, as evidenced

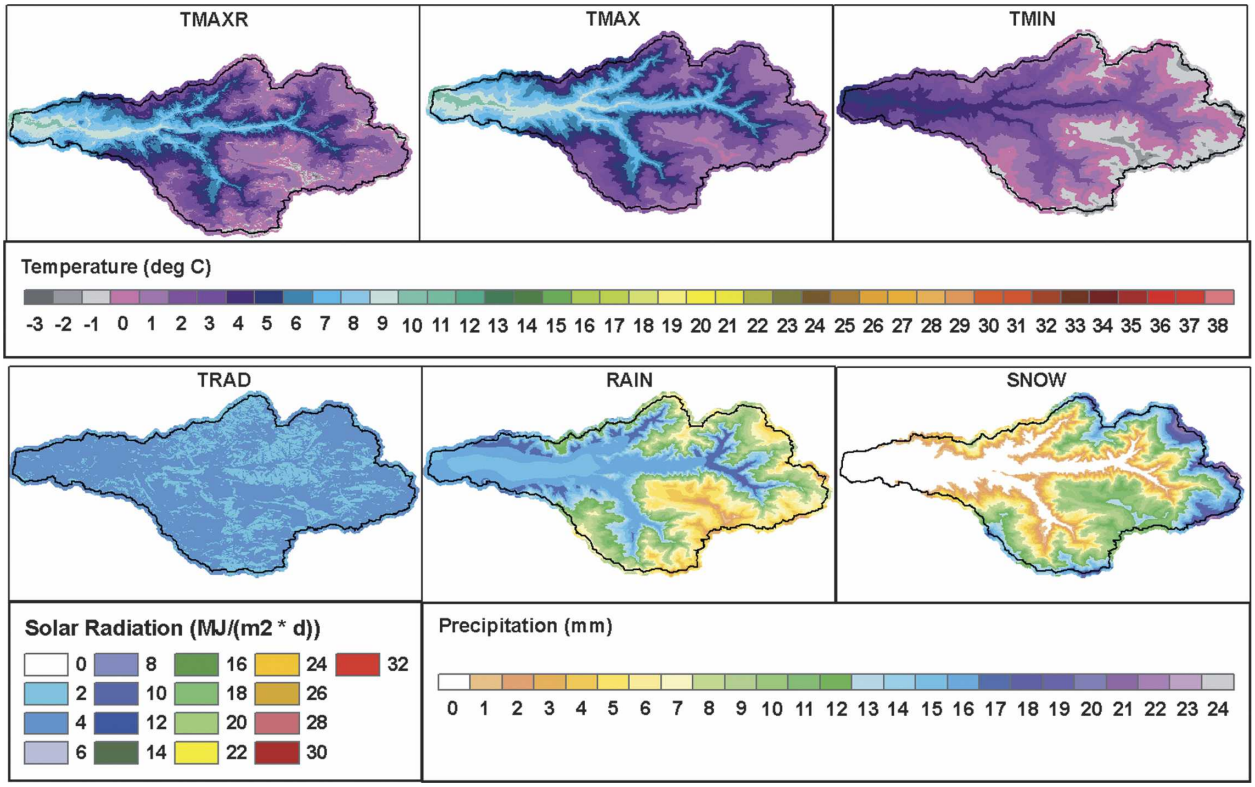

FIG. 10. USSW daily meteorological grids for 17 Feb 2003. Label key: TMAXR = radiation-adjusted maximum temperature, TMAX = maximum temperature, TMIN = minimum temperature, TRAD = total solar radiation, RAIN = rainfall, and SNOW = snowfall.

by a persistent temperature inversion in the morning, which eroded only partially by afternoon. Topographically driven solar radiation variations produced cooler temperatures on north-facing slopes sheltered from the sun relative to those on open, south-facing slopes.

Figure 14 shows daily meteorological grids for 22 December 2003. This was a typical stable, winter day, dominated by temperature inversions. Solar radiation was low but showed considerable topographic differences. A relatively warm "thermal belt" existed at middle elevations, with cooler temperatures above and below this layer.

8. Summary and conclusions

This paper has described the development, application, and assessment of methods to construct daily high-resolution (~50 m) meteorological grids for the 2003 calendar year in the USSW. Meteorological elements included minimum and maximum temperature; total precipitation, rainfall, and snowfall; and solar radiation and radiation-adjusted maximum temperature. Methods discussed include PRISM interpolation of minimum and maximum temperature and precipitation, separation of precipitation into rainfall and snowfall components, IPW solar radiation simulation, and radiation-based adjustments to maximum temperature. PRISM employed pixel-by-pixel regression functions of temperature or precipitation versus elevation and weighted surrounding stations entering the regression function by distance, elevation, topographic position (height above surrounding terrain), and position relative to the local inversion height. The DEM was filtered to a 4-km effective wavelength for precipitation interpolation to match better the scale of elevation effects on precipitation. Separation of precipitation into rainfall and snowfall components used a linear temperature-based function. The Image Processing Workbench was used to simulate solar radiation. IPW used a two-stream radiation model that accounted for the effects of elevation, slope, aspect, reflected radiation, and blocking terrain features. Maximum temperatures were adjusted for varying radiation exposure using equations developed in the nearby H. J. Andrews Experimental Forest.

The restrictive terrain of the USSW promoted cold-air drainage and temperature inversions by reducing large-scale airflow. Inversions were prominent nearly all year for minimum temperature and were noticeable even for maximum temperature during the autumn and winter. These persistent inversions, and the resulting

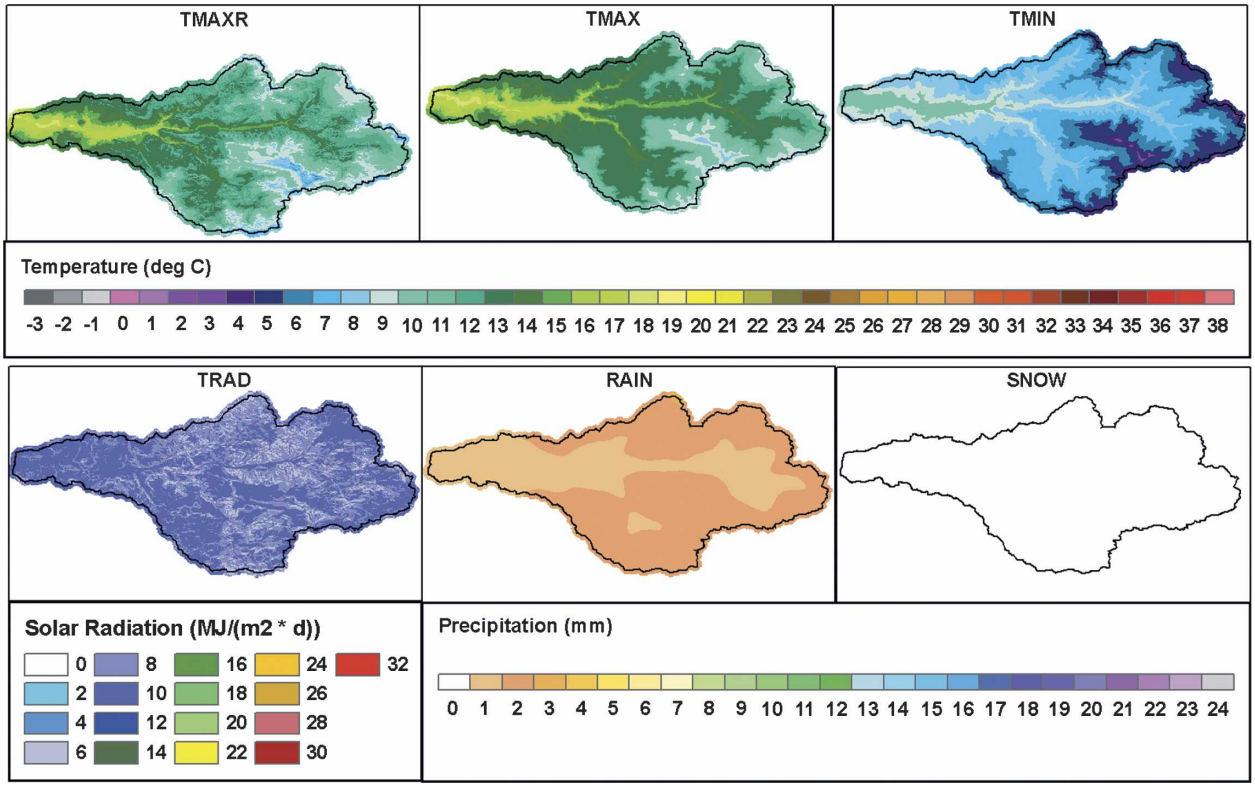

FIG. 11. As in Fig. 10, but for 19 Jun 2003.

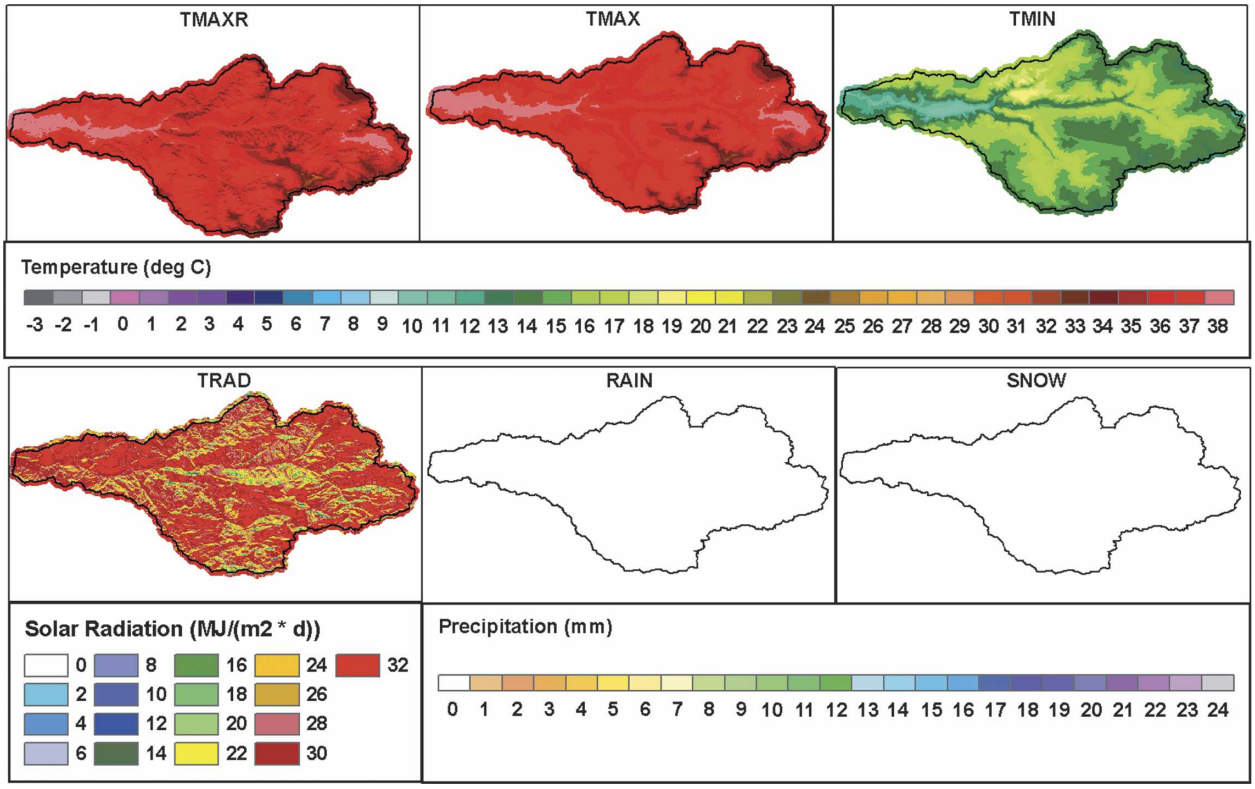

FIG. 12. As in Fig. 10, but for 29 Jul 2003.

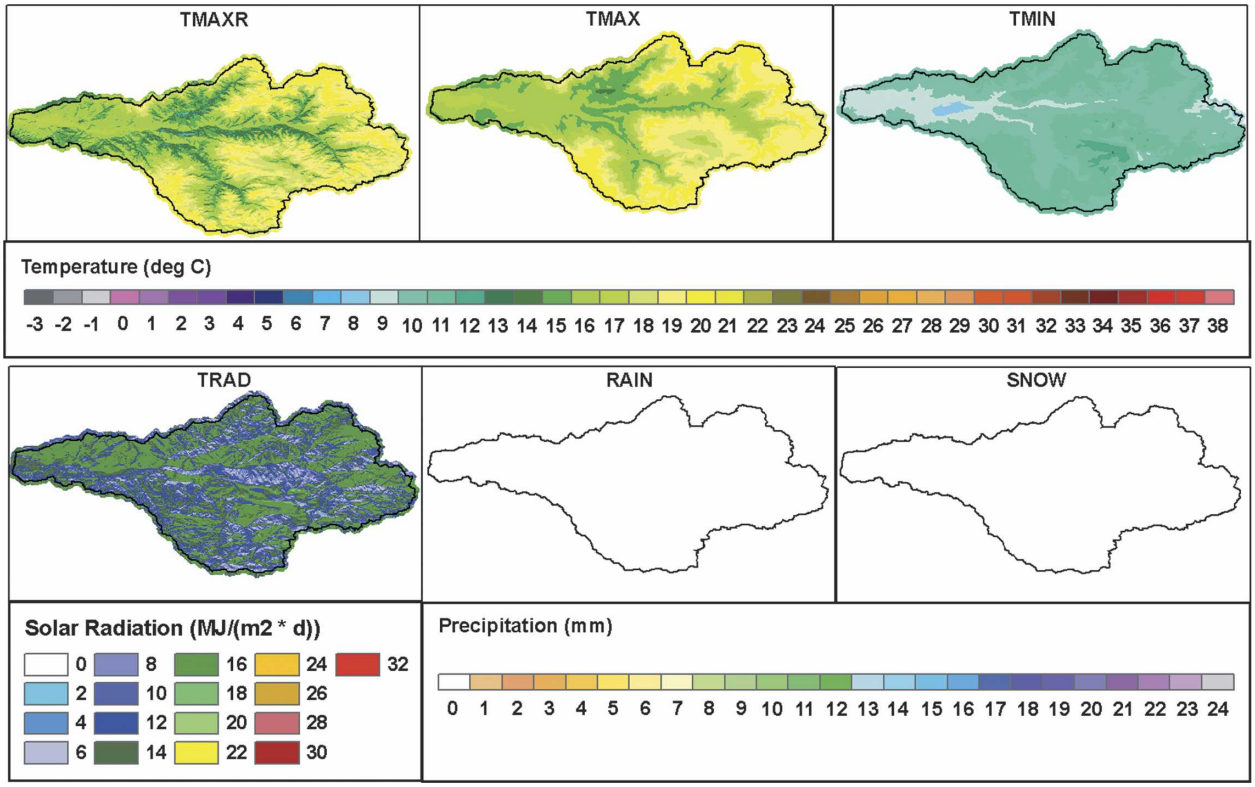

FIG. 13. As in Fig. 10, but for 4 Oct 2003.

complex temperature patterns, were challenging to interpolate accurately. At a minimum, they required an interpolation scheme that simulated sharply changing, nonmonotonic lapse rates and utilized information on typical inversion heights and topographic position, as related to susceptibility to cold drainage. Even so, stations representative of various topographic positions were needed to produce high-quality temperature grids, and it is likely that the grids could have been improved significantly had more station data been available.

The lack of a high-quality observed dataset was a major issue in the interpolation of precipitation and solar radiation. Only the SNOTEL station had the proper equipment to observe precipitation in the form of snow with reasonable accuracy. However, the snow pillow data at this station were not of sufficient quality to allow a daily analysis of the temperature at which snow becomes rain. The lack of a midnight-to-midnight observing day at COOP stations made their use in daily precipitation interpolation difficult and represented the greatest source of uncertainty in the precipitation interpolation. Although solar radiation data were available from three stations within the USSW, only one had data of sufficient quality for use in mapping. In addition, datasets of paired stations with differing solar radiation exposure are needed to quantify better the effects of radiation exposure on daily maximum temperature.

Given the aforementioned shortcomings in data quality and quantity, observed data available for the USSW were superior to those available for most mountainous regions in the western United States. In particular, measurements of solar radiation are often lacking in mountainous environments, requiring the use of estimation methods such as those developed by Scheifinger and Kromp-Kolb (2000) and Thornton et al. (2000).

Resources did not allow this study to be expanded to other commonly used meteorological elements, such as relative humidity. Relative humidity was observed at the EPA stations in the USSW and could be interpolated with the methods described here. There are at least three approaches that might be taken: 1) interpolate relative humidity directly; 2) convert relative humidity to dewpoint and interpolate this element; 3) convert relative humidity to dewpoint depression (difference between dewpoint and ambient temperature) and interpolate this element. In each case, interpolation would be performed primarily by quantifying how the element varied with elevation. As an alternative, meth-

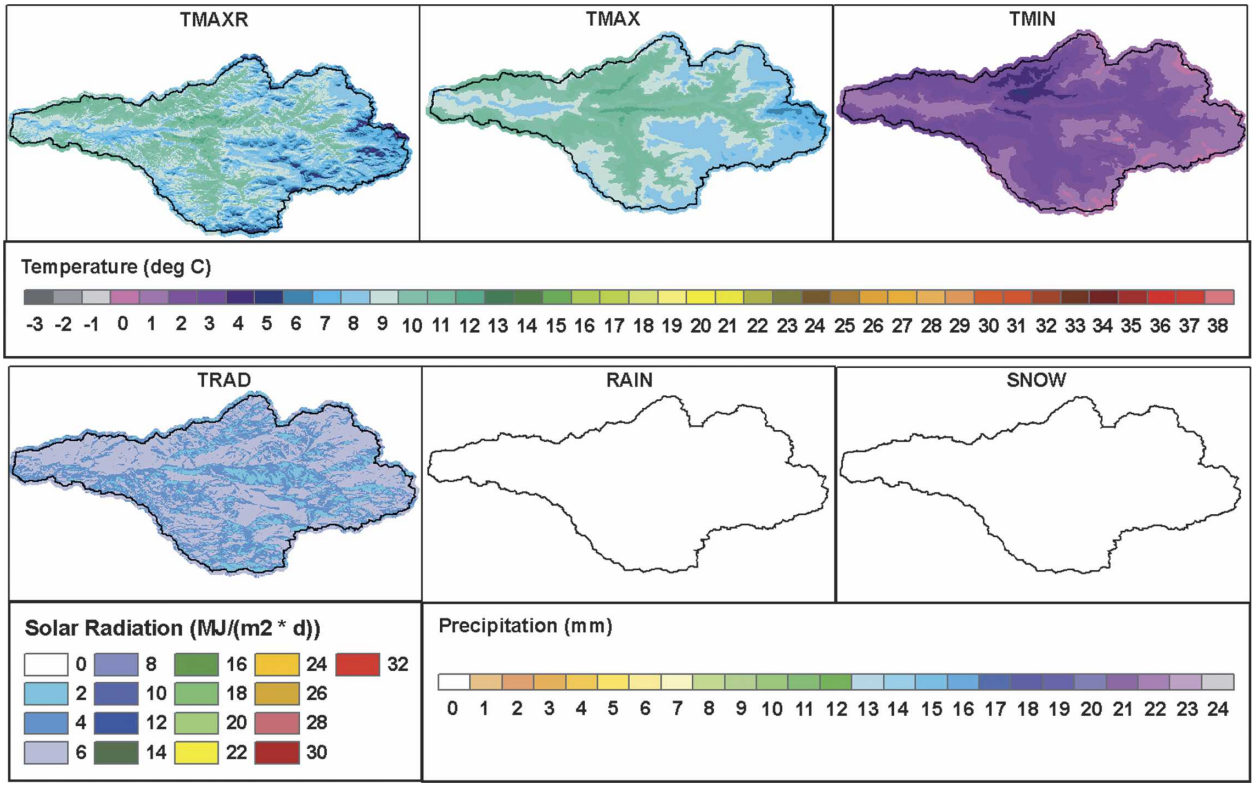

FIG. 14. As in Fig. 10, but for 22 Dec 2003.

ods exist to estimate humidity in the absence of observations, and they can be as simple as setting the dewpoint to the daily minimum temperature. It is unclear whether this method would work well during dry summer months in the USSW, but it may be applicable during the wetter times of the year (Thornton et al. 2000).

Derivative elements useful in ecological modeling, such as potential evapotranspiration (PET), are most effectively interpolated by mapping the individual components involved (e.g., temperature, solar radiation, humidity, wind speed), and calculating the derived value from grid calculations, rather than interpolating directly. This approach allows the use of data from stations that do not observe all of the necessary PET components simultaneously. Wind speed, often desired in PET calculations, is problematic to interpolate from surface observations in this environment, because it is highly variable in complex terrain and can vary dramatically over just a few meters as one moves from sheltered to exposed locations.

Some of the interpolation techniques presented here required significant effort and infrastructure to carry out, and their practical application is limited to locations for which reasonably complete station data are available. However, results from this modeling exercise provide important information on the kinds of spatial meteorological patterns that can be expected to occur in a mountainous catchment such as the USSW, and what can be done to simulate them. It is likely that the USSW is representative of other catchments on the western slopes of the Cascade Mountains and in other mountainous areas of the world.

Acknowledgments. We thank Ron Waschmann for data collection and quality-control procedures for the U.S. Environmental Protection Agency's meteorological stations in the Upper South Santiam Watershed. We also thank Mike Halbleib for preparing the maps for this paper and three anonymous reviewers for their useful comments. This work was funded in part by Contract EP05D000439 from the U.S. Environmental Protection Agency. The information in this document has been subjected to review by EPA's peer and administrative review and was approved for publication.

REFERENCES

Anderson, S. P., and M. F. Baumgartner, 1998: Radiative heating errors in naturally ventilated air temperature measurements made from buoys. *J. Atmos. Oceanic Technol.,* **15,** 157–173.

Barnes, S. L., 1964: A technique for maximizing details in numerical weather map analysis. *J. Appl. Meteor.,* **3,** 396–409.

Barry, R. G., 1992: *Mountain Weather and Climate.* Routledge, 402 pp.

Bolstad, P. V., L. Swift, F. Collins, and J. Regniere, 1998: Measured and predicted air temperatures at basin to regional scales in the southern Appalachian Mountains. *Agric. For. Meteor.,* **91,** 161–176.

Bootsma, A., 1976: Estimating minimum temperature and climatological freeze risk in hilly terrain. *Agric. For. Meteor.,* **16,** 425–443.

Bristow, K., and G. Campbell, 1985: An equation for separating solar radiation into direct and diffuse components. *Agric. For. Meteor.,* **35,** 123–131.

Busing, R. T., A. M. Solomon, R. B. McKane, and C. A. Burdick, 2007: Forest dynamics in western Oregon landscapes: Evaluation and application of an individual-based model. *Ecol. Appl.,* in press.

Chan, S. S., R. W. McCreight, J. D. Walstad, and T. A. Spies, 1986: Evaluating forest vegetative cover with computerized analysis of fisheye photographs. *For. Sci.,* **32,** 1085–1091.

Chung, U., H. H. Seo, K. H. Hwang, B. S. Hwang, J. Choi, J. T. Lee, and J. I. Yun, 2006: Minimum temperature mapping over complex terrain by estimating cold air accumulation potential. *Agric. For. Meteor.,* **137,** 15–24.

Clements, C. B., C. D. Whiteman, and J. D. Horel, 2003: Cold-air-pool structure and evolution in a mountain basin: Peter Sinks, Utah. *J. Appl. Meteor.,* **42,** 752–768.

Daley, R., 1991: *Atmospheric Data Analysis*. Cambridge University Press, 457 pp.

Daly, C., 2002: Variable influence of terrain on precipitation patterns: Delineation and use of effective terrain height in PRISM. Oregon State University, 7 pp. [Available online at http://www.ocs.orst.edu/pub/prism/docs/effectiveterrain-daly.pdf.]

——, 2006: Guidelines for assessing the suitability of spatial climate data sets. *Int. J. Climatol.,* **26,** 707–721.

——, R. P. Neilson, and D. L. Phillips, 1994: A statistical-topographic model for mapping climatological precipitation over mountainous terrain. *J. Appl. Meteor.,* **33,** 140–158.

——, G. H. Taylor, W. P. Gibson, T. W. Parzybok, G. L. Johnson, and P. Pasteris, 2001: High-quality spatial climate data sets for the United States and beyond. *Trans. Amer. Soc. Agric. Eng.,* **43,** 1957–1962.

——, W. P. Gibson, G. H. Taylor, G. L. Johnson, and P. Pasteris, 2002: A knowledge-based approach to statistical mapping of climate. *Climate Res.,* **22,** 99–113.

——, E. H. Helmer, and M. Quinones, 2003: Mapping the climate of Puerto Rico, Vieques, and Culebra. *Int. J. Climatol.,* **23,** 1359–1381.

——, W. P. Gibson, M. Doggett, J. Smith, and G. Taylor, 2004: A probabilistic-spatial approach to the quality control of climate observations. *Proc. 14th Conf. on Applied Climatology,* Seattle, WA, Amer. Meteor. Soc., CD-ROM, 7.3.

Delta-T Devices, 1999: HemiView Canopy Analysis Software. User manual version 2.1, 85 pp. [Available online at http://www.delta-t.co.uk/products.html?product2005092818855.]

Dozier, J., and J. Frew, 1990: Rapid calculation of terrain parameters for radiation modeling from digital elevation data. *IEEE Trans. Geosci. Remote Sens.,* **28,** 963–969.

Dubayah, R., 1994: Modeling a solar radiation topoclimatology for the Rio Grande River basin. *J. Veg. Sci.,* **5,** 627–640.

——, J. Dozier, and F. Davis, 1990: Topographic distribution of clear-sky radiation over the Konza prairie, Kansas. *Water Resour. Res.,* **26,** 679–691.

Easter, M. J., and T. A. Spies, 1994: Using hemispherical photography for estimating photosynthetic photon flux density under canopies and in gaps in Douglas-fir forests of the Pacific Northwest. *Can. J. For. Res.,* **24,** 2050–2058.

Forland, E. J., and I. Hanssen-Bauer, 2000: Increased precipitation in the Norwegian Arctic: True or false? *Climatic Change,* **46,** 485–509.

Franklin, J. F., and C. T. Dyrness, 1988: *Natural Vegetation of Oregon and Washington*. 2d ed. Oregon State University Press, 452 pp.

Frew, J., 1990: The image processing workbench. Ph.D. thesis, University of California, Santa Barbara, 382 pp.

Fuchs, T., J. Rapp, F. Rubel, and B. Rudolf, 2001: Correction of synoptic precipitation observations due to systematic measuring errors with special regard to precipitation phases. *Phys. Chem. Earth,* **26B,** 689–693.

Geiger, R., 1965: *The Climate near the Ground*. Harvard University Press, 611 pp.

Gustavsson, T., M. Karlsson, J. Bogren, and S. Lindqvist, 1998: Development of temperature patterns during clear nights. *J. Appl. Meteor.,* **37,** 559–571.

Hannaway, D. B., and Coauthors, 2005: Forage species suitability mapping for China using topographic, climatic and soils spatial data and quantitative plant tolerances. *Sci. Agric. Sin.,* **4,** 660–667.

Hocevar, A., and J. D. Martsolf, 1971: Temperature distribution under radiation frost conditions in a central Pennsylvania valley. *Agric. For. Meteor.,* **8,** 371–383.

Hubbard, K. G., X. Lin, C. B. Baker, and B. Sun, 2004: Air temperature comparison between the MMTS and the USCRN temperature systems. *J. Atmos. Oceanic Technol.,* **21,** 1590–1597.

Lindkvist, L., T. Gustavsson, and J. Bogren, 2000: A frost assessment method for mountainous areas. *Agric. For. Meteor.,* **102,** 51–67.

Lookingbill, T., and D. Urban, 2003: Spatial estimation of air temperature differences for landscape-scale studies in montane environments. *Agric. For. Meteor.,* **114,** 141–151.

Marks, D., J. Domingo, and J. Frew, 1998: Software tools for hydro-climatic modeling and analysis: Introduction to the Image Processing Workbench (IPW). ARS–USGS version 2. Executive summary, 1 p. [Available online at http://cirque.nwrc.ars.usda.gov/~ipw/exec_summ.html.]

McCutchan, M. H., and D. G. Fox, 1986: Effect of elevation and aspect on wind, temperature and humidity. *J. Climate Appl. Meteor.,* **25,** 1996–2013.

Milewska, E. J., R. F. Hopkinson, and A. Niitsoo, 2005: Evaluation of geo-referenced grids of 1961–1990 Canadian temperature and precipitation normals. *Atmos.–Ocean,* **43,** 49–75.

Oke, T. R., 1987: *Boundary Layer Climates*. Routledge, 435 pp.

Running, S. W., and R. Nemani, 1985: Topographic and microclimate control of simulated photosynthesis and transpiration in coniferous trees. *Proc. Third IUFRO Workshop,* Bermensdorf, Switzerland, IUFRO, 53–60.

Scheifinger, H., and H. Kromp-Kolb, 2000: Modelling global radiation in complex terrain: Comparing two statistical approaches. *Agric. For. Meteor.,* **100,** 127–136.

Sharples, J. J., M. F. Hutchinson, and D. R. Jellet, 2005: On the

horizontal scale of elevation dependence of Australian monthly precipitation. *J. Appl. Meteor.,* **44,** 1850–1865.

Simpson, J. J., G. L. Hufford, C. Daly, J. S. Berg, and M. D. Fleming, 2005: Comparing maps of mean monthly surface temperature and precipitation for Alaska and adjacent areas of Canada produced by two different methods. *Arctic,* **58,** 137–161.

Smith, J. W., 2002: Mapping the thermal climate of the HJ Andrews Experimental Forest, Oregon. M.S. thesis, Department of Geosciences, College of Science, Oregon State University, 222 pp. [Available online at http://www.ocs.orst.edu/pub/smithjw/hja/.]

Thornton, P. E., S. W. Running, and M. A. White, 1997: Generating surfaces of daily meteorological variables over large regions of complex terrain. *J. Hydrol.,* **190,** 214–251.

——, H. Hasenauer, and M. A. White, 2000: Simultaneous estimation of daily solar radiation and humidity from observed temperature and precipitation: An application over complex terrain in Austria. *Agric. For. Meteor.,* **104,** 255–271.

Ting, K. C., and G. A. Giacomelli, 1987: Availability of solar photosynthetically active radiation. *Amer. Soc. Agric. Eng.,* **30,** 1453–1457.

Vales, D. J., and F. L. Bunnell, 1988: Relationships between transmission of solar radiation and coniferous forest stand characteristics. *Agric. For. Meteor.,* **43,** 201–223.